RSC Advances

PAPER

View Article Online
View Journal | View Issue

Check for updates

Cite this: *RSC Adv.*, 2022, **12**, 19869

A PtPdCoCuNi high-entropy alloy nanocatalyst for the hydrogenation of nitrobenzene†

Fagui Lu,[a] Kuan Lu,[b] Gui Zhao,[a] Song Zhou,[c] Bowen He,[a] Yixiao Zhang,[a] Jian Xu,[c] Yongwang Li,[c] Xi Liu *[ad] and Liwei Chen*[ad]

Received 19th May 2022
Accepted 4th July 2022

DOI: 10.1039/d2ra03145k

rsc.li/rsc-advances

High-entropy alloys (HEAs) with multiple elements in near-equiatomic proportions hold great promise in heterogeneous catalysis because of their exceptional physicochemical properties governed by synergy. Herein, we prepared PtPdCoCuNi HEA nanoparticles *via* a one-step colloid-based route and tested their catalytic performance for nitrobenzene hydrogenation to aniline. The SiO_2 supported PtPdCoCuNi displays 93.9% yield of aniline at 80 °C, which is 2.11 times that of PtPd/SiO_2. Even at room temperature, a 47.4% yield of aniline is attained with the PtPdCoCuNi/SiO_2 catalyst. DRIFTS experiments indicate formation of isolated Pt and Pd sites after alloying the transition metals and evidence a stronger interaction between the HEA catalyst and nitrobenzene. Both XPS data and DFT calculations disclose charge transfer to Pt and Pd species, which eventually enhance the interaction between nitrobenzene and the isolated metal sites and the hydrogenation activity as well. The experimental and theoretical results shed light on mechanistic understanding of the unique catalytic performance of the HEA nanocatalyst and pave a new avenue to realize the high catalytic performance of nitrobenzene hydrogenation over well-isolated noble metal sites with specific geometries.

Introduction

Aromatic amines are valuable intermediates for the synthesis of polyurethanes, dyes, rubber additives, pharmaceuticals, explosives, and fine chemicals.[1] The production of aromatic amines from catalytic hydrogenation of nitroaromatics is an important industrial reaction.[2] Tremendous efforts have been made to develop efficient catalysts to achieve highly efficient production of aromatic amines under mild conditions. Pt- and Pd-based catalysts have been extensively investigated for the selective hydrogenation of nitroarenes using molecular hydrogen as an environmentally benign and cheap reducing agent.[1] Improving the activity of catalysts as well as reducing the cost of noble metal-based catalysts are of considerable importance for industrial applications.

In contrast to conventional alloy materials based on single principal elements, high-entropy alloys (HEAs) have recently received considerable attention in various fields because of their unique physical and chemical properties.[3] In principle, HEAs are produced by alloying five or more metal elements in nearly equal proportions (recently extended to 5 to 35 at%) into solid solutions with a high mixing entropy rather than an intermetallic phase.[4] The resulting synergistic effect endows HEAs with high mechanical strength,[5] good thermal stability,[6] and catalytic activity.[7] In particularly, HEAs displayed appraisable catalytic performance in electrocatalytic water splitting,[3,8,9] ammonia oxidation and decomposition,[10,11] and CO_2 reduction.[12] Mechanistic studies suggest that the ligand effect and distortion effect of HEAs, which arise from tuning the composition and geometric properties of HEAs to a large degree, could significantly modify the electronic properties of active sites and consequently improve their catalytic performance.[11] The inherent synergy effect of HEAs provides possibility to boost the catalytic activity by combining suitable metals.

However, the preparation of uniform HEA nanoparticles is challenging because the difference in reduction potentials and rates of different metal precursors can easily lead to phase separation. The conventional impregnation chemical strategy, which was used to produce supported HEA nanoparticles,[12] has obvious disadvantages in terms of size and composition of the nanoparticles. Although HEA nanoparticles can be produced by carbothermal shock method,[10,11] this method does not allow scaled-up production due to high requirements for the instrument and thermal stability of supports. Subsequently, fast moving bed pyrolysis,[3] metal–organic framework pyrolysis,[9] and

[a]*School of Chemistry and Chemical Engineering, In-situ Center for Physical Sciences, Frontiers Science Center for Transformative Molecules, Shanghai Jiao Tong University, Shanghai 200240, China. E-mail: liuxi@sjtu.edu.cn; lwchen2018@sjtu.edu.cn*

[b]*State Key Laboratory of Coal Conversion, Institute of Coal Chemistry, Chinese Academy of Sciences, Taiyuan 030001, China*

[c]*SynCat@Beijing Synfuels China Technology Co. Ltd, Beijing 101407, China*

[d]*Shanghai Jiao Tong University, China Shanghai Electrochemical Energy Device Research Center (SEED), Shanghai 200240, China*

† Electronic supplementary information (ESI) available. See https://doi.org/10.1039/d2ra03145k

Open Access Article. Published on 07 July 2022. Downloaded on 2/8/2026 10:24:19 AM.
This article is licensed under a Creative Commons Attribution-NonCommercial 3.0 Unported Licence.

Open Access Article. Published on 07 July 2022. Downloaded on 2/8/2026 10:24:19 AM.
This article is licensed under a Creative Commons Attribution-NonCommercial 3.0 Unported Licence.

synergistic confinement strategy[13] were explored as alternative synthetic approaches. Unfortunately, the experimental conditions crucially limit their practical applications.

Nowadays, the colloid solvothermal method has been widely used in the synthesis of bimetallic or trimetallic alloy nanoparticles.[14,15] This one-pot colloid-based approach can integrate distinct metal elements into nanocrystals to form well-defined structure, by which allows the preparation of nanoparticles with uniform chemical compositions and homogenous size distributions.[16,17] Therefore, a general colloidal approach to synthesis of HEA nanoparticles should be developed to provide new opportunities in catalyst design and beyond.[8]

In this paper, small PtPdCoCuNi HEA nanoparticles were successfully prepared by a one-pot solvothermal synthesis method and deposited on SiO_2 to prepare a PtPdCoCuNi/SiO_2 catalyst with uniform dispersion of HEA nanoparticles. The catalytic performance of the PtPdCoCuNi/SiO_2 catalyst for nitrobenzene hydrogenation was tested and compared to counterparts with fewer metal components. The PtPdCoCuNi/SiO_2 catalyst exhibits high activity even at room temperature. The catalyst was characterized by a series of techniques, including HRSTEM, XRD, XPS, and DRIFTS, to obtain mechanistic understanding of the structure–activity relationship of the HEA catalyst. Both experimental and theoretical results evidence the formation of isolated Pt and Pd active sites in HEA and the resulting charge-transfer from the cheap transition metals to the noble metals, which suggests that the modulated electronic structure could promote adsorption of nitrobenzene on Pt/Pd active sites and eventually enhance nitrobenzene hydrogenation activity.

Results and discussion

The morphology of the as-prepared PtPdCoCuNi nanoparticles was characterized by transmission electron microscopy (TEM). As shown in Fig. 1A, the nanoparticles are uniform in terms of morphology and size. An average diameter of the PtPdCoCuNi nanoparticles is around 7.1 ± 3.2 nm with a narrow size distribution. A selected area electron diffraction (SAED) pattern of the PtPdCoCuNi nanoparticles with clear diffraction polycrystalline rings (Fig. 1C) is indexed to face-centered cubic (fcc) structure. As seen in a high-resolution TEM (HRTEM) image (Fig. 1B), the measured lattice-fringe distances of the PtPdCoCuNi nanoparticles are 0.22 and 0.19 nm, corresponding to the (111) and (002) facets of fcc, respectively. After the deposition of PtPdCoCuNi nanoparticles on SiO_2 and following reduction at 160 °C under H_2 atmosphere, the morphology and size of supported PtPdCoCuNi nanoparticles keep unchanged, which are uniformly dispersed on SiO_2 without obvious aggregation (Fig. 1D and 2A). A HRTEM image (Fig. 1E) of the post-treated nanoparticles validates negligible differences in the crystal structure. An X-ray diffraction (XRD) pattern of the PdPdCoCuNi/SiO_2 catalyst is shown in Fig. 1F, in which diffraction peaks located at 40.9°, 47.5°, and 69.5° should be assigned to the (111), (002), and (022) facets, respectively (fcc Pd, JCPDF: 96-101-1111). Rietveld refinement analysis of the diffraction result indicates the formation of fcc structure with a lattice parameter of $a = 3.838$ Å. This value is between 3.908 Å (for fcc Pd, JCPDF: 96-101-1111) and 3.524 Å (for fcc Ni, JCPDF: 96-151-2527), suggesting presence of large local structural distortion. When the period 4 elements were alloyed into PdPt bimetallic matrix in sequence to form tri-, quad-, and quin-metallic alloy (see Fig. S3 and S4†), a gradual decrease in the value was observed, indicating apparent lattice shrinks during the progressive replacement of Pt or Pd atoms with heteroatoms.

An atomically resolved scanning transmission electron microscopy annular dark field (STEM-ADF) image of a HEA nanoparticle (Fig. 2B) discloses its poly crystalline nature. The corresponding energy-dispersive X-ray spectroscopy (EDS) elemental mapping displays that each metal element (Pt, Pd, Co, Cu, and Ni) is evenly distributed throughout the entire nanoparticle, confirming the successful synthesis of the HEA alloy. Inductively coupled plasma atomic emission spectroscopy (ICP–AES) data (Fig. S5†) show that the mole ratios of these five metals (Pt, Pd, Co, Cu, and Ni) range from 14% to 24%, which is consistent with the definition of HEA. We also calculated the thermodynamic properties of the synthetic PtPdCoCuNi nanoparticles based on the equations proposed by Xie *et al.*, who

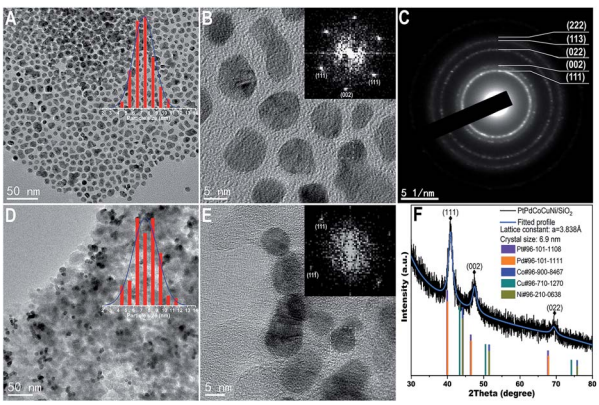

Fig. 1 (A) TEM image (inset: particle size distribution), (B) HRTEM image (inset: FFT pattern from the white dotted box area), and (C) SAED pattern of PtPdCoCuNi nanoparticles; (D) TEM image (inset: particle size distribution), (E) HRTEM image (inset: FFT pattern from the white dotted box area), and (F) XRD pattern of PtPdCoCuNi/SiO_2 catalyst, the crystal size of about 6.9 nm is determined from the XRD result, which is consistent with the TEM result.

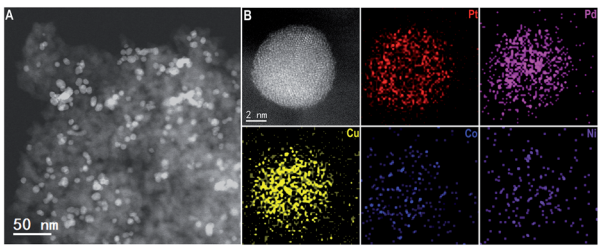

Fig. 2 (A) STEM-ADF image of PtPdCoCuNi/SiO_2 catalyst; (B) STEM-ADF image and corresponding EDS elemental mapping of PtPdCoCuNi/SiO_2 catalyst.

© 2022 The Author(s). Published by the Royal Society of Chemistry

Open Access Article. Published on 07 July 2022. Downloaded on 2/8/2026 10:24:19 AM.
This article is licensed under a Creative Commons Attribution-NonCommercial 3.0 Unported Licence.

supposed that the formation of HEA requires an atomic size difference $\delta \leq 6.6\%$ and an enthalpy of mixing ΔH_{mix} between -11.6 and 3.2 kJ mol^{-1}.[11] In the present study, it is calculated that $\delta = 5.3\%$, $\Delta H_{mix} = -1.35$ kJ mol^{-1}, $\Delta S_{mix} = 13.26$ J mol^{-1} K^{-1}, and $\Delta G_{mix} = -7.62$ kJ mol^{-1} for the PtPdCoCuNi nanoparticles, in good agreement with the reference.

X-ray photoelectron spectroscopy (XPS) was performed to explore the valence states of Pt, Pd, Co, Cu, and Ni in the PtPdCoCuNi/SiO_2 catalyst and its counterparts with fewer components. For the quin-metallic sample, the Pt $4f_{7/2}$ and Pt $4f_{5/2}$ peaks of the quin-metallic sample (Fig. S6A†) are centered at 70.2 and 73.6 eV respectively, which should be attributed to metallic Pt.[18] The Pd $3d_{5/2}$ and Pd $3d_{3/2}$ doublet peaks (Fig. S6B†) are located at 334.5 and 339.8 eV, respectively, associated with metallic Pd.[19] The binding energy of Co $2p_{3/2}$ (Fig. S6C†) is about 778.5 eV, which is consistent with metallic Co.[20] The Cu $2p_{3/2}$ and Cu $2p_{1/2}$ (Fig. S6D†) with binding energies of 931.7 and 951.5 eV are attributed to metallic state of Cu.[21] Furthermore, the Auger Cu LMM spectrum (Fig. S6E†) at 918.9 eV confirms the metallic state of Cu species.[14] The binding energy of Ni $2p_{3/2}$ at approximately 853.0 eV (Fig. S6F†) is attributed to metallic Ni.[22] The XPS analysis confirms that all the constituent elements of Pt, Pd, Co, Cu, and Ni in the HEA nanoparticles are mainly in metallic states. However, both peaks of Pt 4f (Fig. 3A) and Pd 3d (Fig. 3B) gradually shift towards lower binding energies associated with incrementally alloying of Co/Cu/Ni into PtPd matrix one-by-one, indicating the increasing charge transfer to Pt and Pd. Similar charge transfer from Co to noble metal Pd has previously been observed in CoPd alloy, disclosing that introducing cheap transition metal can alter the electronic state of Pd species, and subsequently affect their catalytic performance.[23] Clearly, the characterization data validate the obvious structural and electronic alternations in the HEA nanoparticles, which should significantly influence their physicochemical properties, like catalytic reactivity.

In this study, hydrogenation of nitrobenzene to aniline was chosen as a model reaction to demonstrate the catalytic advantage of PtPdCoCuNi/SiO_2 over the bi-, tri-, quad-metallic alloy catalysts. Fig. 4A shows yields of aniline over these PtPd-based samples and their monometallic counterparts. Apparently, the hydrogenation reaction hardly occurs over the unary cheap transition metal Co/SiO_2, Cu/SiO_2, or Ni/SiO_2 catalyst, as yields of aniline are less than 2.2% (Fig. 4A). The unary noble metal Pt/SiO_2 and Pd/SiO_2 catalysts exhibit relatively high

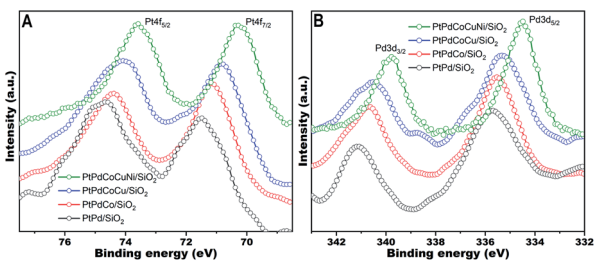

Fig. 3 Pt 4f and Pd 3d XPS spectra of PtPd/SiO_2, PtPdCo/SiO_2, PtPdCoCu/SiO_2, and PtPdCoCuNi/SiO_2 catalysts.

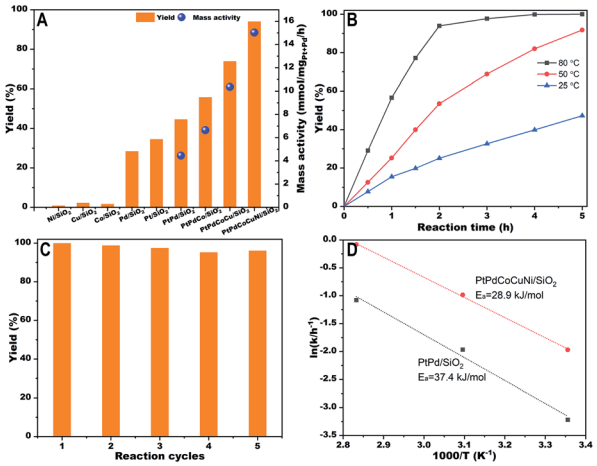

Fig. 4 (A) Aniline yield and mass productivity over unary, PtPd/SiO_2, PtPdCo/SiO_2, PtPdCoCu/SiO_2, and PtPdCoCuNi/SiO_2 catalysts at 80 °C within 2 h; (B) aniline yield over PtPdCoCuNi/SiO_2 catalyst at 80, 50, and 25 °C; (C) cycling tests for nitrobenzene hydrogenation over PtPdCoCuNi/SiO_2 catalyst at 80 °C within 3 h; (D) arrhenius plots obtained from aniline yield data over PtPdCoCuNi/SiO_2 and PtPd/SiO_2 catalysts. Reaction conditions: 50 mg catalyst, 600 rpm, 3 MPa H_2, 30 mL cyclohexane, 20 mmol nitrobenzene.

activity, which is slightly lower than that of the binary PtPd/SiO_2 catalyst. These results indicate that Pt and Pd are the main active species in the hydrogenation of nitrobenzene. After alloying Co, Cu, and Ni in sequence, the yield of aniline increases from 44.4% (PtPd/SiO_2) to 55.6% (PtPdCo/SiO_2), and 73.7% (PtPdCoCuNi/SiO_2), and finally reaches 93.9% for PtPdCoCuNi/SiO_2 with a mass productivity of 15.0 $mmol_{aniline}$ mg_{Pt+Pd}^{-1} h^{-1}, which is 1.46, 2.27, and 3.41 times to those of PtPdCoCu/SiO_2 (10.3 $mmol_{aniline}$ mg_{Pt+Pd}^{-1} h^{-1}), PtPdCo/SiO_2 (6.6 $mmol_{aniline}$ mg_{Pt+Pd}^{-1} h^{-1}), and PtPd/SiO_2 (4.4 $mmol_{aniline}$ mg_{Pt+Pd}^{-1} h^{-1}), respectively. All these catalysts gave almost 100% selectivity to the target product aniline. The turnover frequency (TOF) of PtPdCoCuNi/SiO_2 catalyst was higher than the values achieved by some most active Pt or Pd-based catalysts (Table S1†). In addition, the PtPdCoCuNi/SiO_2 catalyst also exhibited high activity for hydrogenation of other substituted nitroarenes to the corresponding aromatic amines (Fig. S8†). The catalytic performance definitely confirms that the continuously alloying inactive transition metals greatly manipulate their catalytic performance. The excellent performance of PtPdCoCuNi/SiO_2 toward nitrobenzene reduction could be ascribed to the synergistic effect obtained from the combination of elements comprising the HEAs.[8,12]

The effects of reaction temperature and time on hydrogenation of nitrobenzene to aniline over PtPdCoCuNi/SiO_2 were also investigated in the present work. As shown in Fig. 4B, when the reaction temperature decreases from 80 to 50 °C, the two-hour yield of aniline decreases from 93.9% to 53.5%. But even at room temperature, the catalyst still displays marked activity toward nitrobenzene hydrogenation with a two-hour yield of 25.1%. Extending the reaction time favors the productivity of aniline and a 47.3% aniline yield is achieved at room temperature after 5 hours reaction without byproducts. After 5 hours'

© 2022 The Author(s). Published by the Royal Society of Chemistry

Open Access Article. Published on 07 July 2022. Downloaded on 2/8/2026 10:24:19 AM.
This article is licensed under a Creative Commons Attribution-NonCommercial 3.0 Unported Licence.

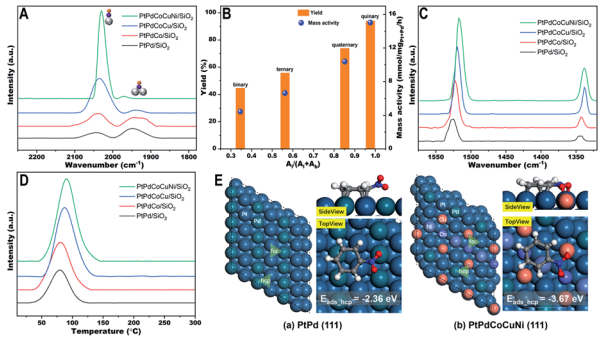

Fig. 5 (A) Normalized CO-DRIFTS spectra, (B) relationships between the $A_l/(A_l + A_b)$ and catalytic performance, (C) normalized nitrobenzene-DRIFTS spectra, and (D) normalized nitrobenzene-TPD of PtPd/SiO_2, PtPdCo/SiO_2, PtPdCoCu/SiO_2, and PtPdCoCuNi/SiO_2 catalysts; (E) the (111) surface model and the corresponding hcp adsorption structure of nitrobenzene on (a) PtPd and (b) PtPdCoCuNi, respectively.

reaction, a complete conversion is obtained at 80 °C and a yield of 91.7% is obtained at 50 °C, respectively. The mass productivity of PtPdCoCuNi/SiO_2 reaches 5.9 and 3.0 $mmol_{aniline}$ mg_{Pt+Pd}^{-1} h^{-1} at 50 and 25 °C, respectively. The supported PtPdCoCuNi catalysts with different metal loading (0.1 wt% to 4.0 wt%) for the hydrogenation of nitrobenzene were also tested, showing a typical volcano-shaped activity with an optimal loading amount of 2.0 wt% (Fig. S11†). Moreover, the influence of content of the cheap transition metals in nanoparticles on overall catalytic performance was examined, indicating that the catalytic performance dropped rapidly when the concentration of CoCuNi increased (Fig. S12†). The PtPdCoCuNi/SiO_2 catalyst displays considerable reusability as the activity of PtPdCoCuNi/SiO_2 decreases marginally after five cycles (Fig. 4C). The morphology of used PtPdCoCuNi/SiO_2 catalyst is well maintained, and no obvious aggregation of nanoparticles appears after the reaction (Fig. S13A†). In addition, EDS elemental mapping evidences the structural stability of HEA nanoparticles (Fig. S13B†). No metal component (Pt, Pd, Co, Cu, and Ni) was detected in the reaction solution from the ICP-AES results. The slight decrease of catalytic activity may be due to the blockage of pores (Fig. S2†). These results validate that the PtPdCoCuNi/SiO_2 HEA catalyst has good reusability and stability in hydrogenation of nitrobenzene. Linear relationships between $-\ln(1 - \text{yield})$ and reaction time are obtained over PtPdCoCuNi/SiO_2 and PtPd/SiO_2 catalysts, which are fitted well with the first-order reaction kinetics (Fig. S14 and S15†), suggesting that the nitrobenzene hydrogenation follows a similar reaction pathway over the two catalysts.[24] According to the Arrhenius plot, the apparent activation energy (E_a) is determined to be 28.9 kJ mol^{-1} over PtPdCoCuNi/SiO_2 catalyst for the hydrogenation of nitrobenzene to aniline (Fig. 4D), which is slightly lower than the apparent activation energy of PtPd/SiO_2 catalyst (37.4 kJ mol^{-1}). The obtained activation energies is quite similar to the value previously reported in the literature,[25] suggesting the catalytic hydrogenation reaction over the HEA catalyst follows the similar reaction pathway.[25,26]

Conclusions

Considering the similar size and morphology between PtPd and PtPdCoCuNi nanoparticles, the higher activity of PtPdCoCuNi/SiO_2 catalyst should be largely attributed to promoted chemisorption over active sites.

To further explore the structure–activity relationship of these PtPd-based samples for the hydrogenation reaction, diffuse reflectance infrared Fourier transform spectroscopy (DRIFTS) of CO absorption was performed (Fig. 5A). In principle, frequencies of CO adsorbed on metal sites are determined by adsorption types, including low-coordinated sites or even single atoms responsible for linear-type CO adsorption (above 2000 cm^{-1}) and close-packed surface for bridging-type adsorption (below 1980 cm^{-1}).[27] With alloying more transition metals into the PtPd matrix, intensity of the linear CO adsorption peak and a proportion of peak area of the linear adsorption to that of total CO adsorption ($A_l/(A_l + A_b)$) increase progressively. This result indicates that Pt or Pd assembly is separated incrementally by the incorporation of cheap transition metals and consequently turned into isolated Pt or Pd sites, resulting in decrease in bridging CO adsorption as well as increase in linear CO adsorption.[28] The isolated Pt or Pd sites can serve as active sites for selective hydrogenation of unsaturated aromatic nitrogen compounds.[29] Moreover, the linear CO adsorption band is redshifted with increasing metal composition, indicating modulated interaction between adsorbed CO and Pt or Pd active sites. Moreover, the increased electron density of Pt/Pd evidenced by the XPS results can enhance the electron feedback from the d-orbital of metallic Pt/Pd to the antibonding orbital (π^*) of CO and consequently weaken the C≡O bond, leading to a redshift of the linear CO adsorption stretching band.[27] The components of Co/Cu/Ni serve a dual role in isolating Pt/Pd and increasing electron density of Pt/Pd. The aniline yield and mass productivity are found to be almost linearly correlated proportionally with the ratio of linear CO adsorption ($A_l/(A_l + A_b)$) for the PtPd-based catalysts (Fig. 5B), indicating that the modulated structural and electronic properties of Pt and Pd should be the main reason for the enhanced catalytic performance. In order to examine the correlation, DRIFTS spectra of nitrobenzene were also studied to disclose the interaction between nitrobenzene and active sites and thus to better understand the origin of the excellent catalytic performance of PtPdCoCuNi/SiO_2 catalyst. As shown in Fig. 5C, two characteristic absorbance peaks located at about 1526 and 1344 cm^{-1} are observed, which are assigned to the asymmetric and symmetric stretching vibrations of nitro group, respectively.[1] Similar to the CO-DRIFTS profiles, the promoted interaction between Pt/Pd active sites and adsorbed nitrobenzene was evidenced by the down-shifting of the corresponding vibrations, since the redshift of the characteristic nitro peaks should be attributed to electron transfer from metallic Pt/Pd to nitro group.[30] Furthermore, nitrobenzene-TPD experiments were conducted to investigate the enhanced chemisorption of nitrobenzene on PtPd-based catalysts (Fig. 5D). The peak area and desorption temperature along with the increase in metal composition, confirming that there is the

© 2022 The Author(s). Published by the Royal Society of Chemistry

Open Access Article. Published on 07 July 2022. Downloaded on 2/8/2026 10:24:19 AM.
This article is licensed under a Creative Commons Attribution-NonCommercial 3.0 Unported Licence.

maximum chemisorption of nitrobenzene on the PtPdCoCuNi/SiO_2 catalyst over other PtPd-based catalysts. Both nitrobenzene-DRIFTS and TPD results are consistent with the CO-DRIFTS and XPS data, indicating that the isolated electron-rich Pt and Pd sites are preferable for adsorption and activation of nitrobenzene for the subsequent hydrogenation reaction. Clearly, the addition of Co/Cu/Ni increases the dispersion of Pt/Pd, generating isolated Pt and Pd sites on PtPd-based catalysts. On the other hand, the incorporation of Co/Cu/Ni also increases the electron density of Pt/Pd, thus enhancing interaction between nitrobenzene and the isolated metal sites.

DFT calculations were performed to obtain insightful understanding of the electronic properties of PtPdCoCuNi in comparison with PtPd. Differential charge distributions of the two models (Fig. S16†) confirm the relatively nucleophilic nature of Pt and Pd sites (0.11*e* and 0.05*e*, respectively) in the PtPdCoCuNi matrix compared with the bimetallic PtPd system, which is in a good agreement with XPS data. In addition, the adsorption energy of nitrobenzene on PtPd and PtPdCoCuNi was calculated to identify the interaction between these active sites and the reactant molecule. All models consisted of six layers with $p(6 \times 6)$: the top three layers were relaxed and the bottom three layers were fixed. The HEA model was simply represented by the top one-layer alloy atoms, as shown in Fig. 5E. Lower adsorption energy indicates stronger adsorption. The results show that the lowest adsorption energy of nitrobenzene on the PtPd(111) surface was −2.36 eV for the hcp site, and the most stable adsorption structure of nitrobenzene on the PtPdCoCuNi(111) surface was also on the hcp site (−3.67 eV). The adsorption energy of nitrobenzene on PtPd was rather high, accounting for the lower hydrogenation activity observed for the PtPd/SiO_2 catalyst. In contrast, nitrobenzene was strongly adsorbed on the PtPdCoCuNi surface. The lower adsorption energy/stronger adsorption of nitrobenzene on the PtPdCoCuNi(111) surface indicates that nitrobenzene is easily attached to PtPdCoCuNi/SiO_2 with the highest possibility for reaction, which could explain the higher hydrogenation activity of PtPdCoCuNi/SiO_2, validating that the interaction between PtPdCoCuNi/SiO_2 and nitrobenzene is stronger than that with PtPd/SiO_2. The comprehensive experimental and theoretical results prove that the formation of the HEA nanocatalyst creates highly-isolated and nucleophilic Pt and Pd active sites, and eventually modulates the chemisorption of nitrobenzene over the active sites and thereby its catalytic performance for the selective hydrogenation.

In summary, we have successfully synthesized PtPdCoCuNi HEA nanoparticles using a simple one-step solvothermal method. The PtPdCoCuNi/SiO_2 catalyst exhibits the high catalytic activity for hydrogenation of nitrobenzene to aniline. The HEA nanocatalyst displays much better catalytic performance than the monometallic catalysts and other PtPd alloy catalysts. Even at room temperature, an aniline yield of 47.3% is achieved after 5 hours of reaction. The enhanced activity of PtPdCoCuNi/SiO_2 is attributed to the high dispersion of Pt and Pd in HEA and the arising synergistic electronic properties of the formed active sites. This work not only provides a viable synthetic route for the fabrication of HEA nanoparticles, but also provides detailed mechanistic understanding of this unique catalyst. We expect that this new synthetic strategy will facilitate the design and synthesis of new HEA nanoparticles for catalysis or other applications.

Conflicts of interest

There are no conflicts to declare.

Acknowledgements

This work was financially supported by the National Key R&D Program of China (2021YFA1500300) and the National Natural Science Foundation of China (Grant No. 21991153, 21991150, and 22072090). The authors acknowledge support from Synfuels China Technology Co. Ltd (Beijing).

Notes and references

1 Q. Zhang, J. Bu, J. Wang, C. Sun, D. Zhao, G. Sheng, X. Xie, M. Sun and L. Yu, *ACS Catal.*, 2020, **10**, 10350–10363.
2 D. Formenti, F. Ferretti, F. K. Scharnagl and M. Beller, *Chem. Rev.*, 2019, **119**, 2611–2680.
3 S. Gao, S. Hao, Z. Huang, Y. Yuan, S. Han, L. Lei, X. Zhang, R. Shahbazian-Yassar and J. Lu, *Nat. Commun.*, 2020, **11**, 2016.
4 Y. Xin, S. Li, Y. Qian, W. Zhu, H. Yuan, P. Jiang, R. Guo and L. Wang, *ACS Catal.*, 2020, **10**, 11280–11306.
5 S. W. Wu, G. Wang, Q. Wang, Y. D. Jia, J. Yi, Q. J. Zhai, J. B. Liu, B. A. Sun, H. J. Chu, J. Shen, P. K. Liaw, C. T. Liu and T. Y. Zhang, *Acta Mater.*, 2019, **165**, 444–458.
6 Y. Yao, Z. Liu, P. Xie, Z. Huang, T. Li, D. Morris, Z. Finfrock, J. Zhou, M. Jiao, J. Gao, Y. Mao, J. Miao, Z. Peng, R. Shahbazian-Yassar, C. Wang, G. Wang and L. Hu, *Sci. Adv.*, 2020, **6**, eaaz0510.
7 K. Zhao, X. Li and D. Su, *Acta Phys.-Chim. Sin.*, 2021, **37**, 2009077.
8 H. Li, Y. Han, H. Zhao, W. Qi, D. Zhang, Y. Yu, W. Cai, S. Li, J. Lai, B. Huang and L. Wang, *Nat. Commun.*, 2020, **11**, 5437.
9 K. Huang, B. Zhang, J. Wu, T. Zhang, D. Peng, X. Cao, Z. Zhang, Z. Li and Y. Huang, *J. Mater. Chem. A*, 2020, **8**, 11938–11947.
10 Y. Yao, Z. Huang, P. Xie, S. D. Lacey, R. J. Jacob, H. Xie, F. Chen, A. Nie, T. Pu, M. Rehwoldt, D. Yu, M. R. Zachariah, C. Wang, R. Shahbazian-Yassar, J. Li and L. Hu, *Science*, 2018, **359**, 1489–1494.
11 P. Xie, Y. Yao, Z. Huang, Z. Liu, J. Zhang, T. Li, G. Wang, R. Shahbazian-Yassar, L. Hu and C. Wang, *Nat. Commun.*, 2019, **10**, 4011.
12 K. Mori, N. Hashimoto, N. Kamiuchi, H. Yoshida, H. Kobayashi and H. Yamashita, *Nat. Commun.*, 2021, **12**, 3884.
13 H. Li, H. Zhu, Q. Shen, S. Huang, S. Lu, P. Ma, W. Dong and M. Du, *Chem. Commun.*, 2021, **57**, 2637–2640.
14 F. Lu, S. Zhou, S. Li, H. Jiang, B. He, J. Qi, Y. Zhang, X. Liu, J. Xu, Y. Li, X. Liu and L. Chen, *J. Phys. Chem. C*, 2021, **125**, 23205–23211.

© 2022 The Author(s). Published by the Royal Society of Chemistry

Open Access Article. Published on 07 July 2022. Downloaded on 2/8/2026 10:24:19 AM.
This article is licensed under a Creative Commons Attribution-NonCommercial 3.0 Unported Licence.

15 Y. Tuo, Q. Lu, C. Chen, T. Liu, Y. Pan, Y. Zhou and J. Zhang, *RSC Adv.*, 2021, **11**, 26326–26335.
16 A. Holm, E. D. Goodman, J. H. Stenlid, A. Aitbekova, R. Zelaya, B. T. Diroll, A. C. Johnston-Peck, K.-C. Kao, C. W. Frank, L. G. M. Pettersson and M. Cargnello, *J. Am. Chem. Soc.*, 2020, **142**, 14481–14494.
17 L. Lin, J. Liu, X. Liu, Z. Gao, N. Rui, S. Yao, F. Zhang, M. Wang, C. Liu, L. Han, F. Yang, S. Zhang, X. D. Wen, S. D. Senanayake, Y. Wu, X. Li, J. A. Rodriguez and D. Ma, *Nat. Commun.*, 2021, **12**, 6978.
18 W. Xu, J. Chang, Y. Cheng, H. Liu, J. Li, Y. Ai, Z. Hu, X. Zhang, Y. Wang, Q. Liang, Y. Yang and H. Sun, *Nano Res.*, 2021, **15**, 965–971.
19 Y. Bao and L. Feng, *Acta Phys.-Chim. Sin.*, 2021, **37**, 2008031.
20 Q. Jiang, W. Luo, Y. Piao, H. Matsumoto, X. Liu, A. Züttel, K. Parkhomenko, C. Pham-Huu and Y. Liu, *ACS Catal.*, 2021, **11**, 8087–8096.
21 Y.-B. Chang, C. Zhang, X.-L. Lu, W. Zhang and T.-B. Lu, *Nano Res.*, 2021, **15**, 195–201.
22 Y. H. Ahmad, A. T. Mohamed, A. Kumar and S. Y. Al-Qaradawi, *RSC Adv.*, 2021, **11**, 33734–33743.
23 W. Ye, X. Shi, Y. Zhang, C. Hong, C. Wang, W. M. Budzianowski and D. Xue, *ACS Appl. Mater. Interfaces*, 2016, **8**, 2994–3002.
24 E. S. Gutterød, S. Øien-Ødegaard, K. Bossers, A.-E. Nieuwelink, M. Manzoli, L. Braglia, A. Lazzarini, E. Borfecchia, S. Ahmadigoltapeh, B. Bouchevreau, B. T. Lønstad-Bleken, R. Henry, C. Lamberti, S. Bordiga, B. M. Weckhuysen, K. P. Lillerud and U. Olsbye, *Ind. Eng. Chem. Res.*, 2017, **56**, 13206–13218.
25 M. Turáková, T. Salmi, K. Eränen, J. Wärnå, D. Y. Murzin and M. Králik, *Appl. Catal., A*, 2015, **499**, 66–76.
26 L. Zhang, J. Jiang, W. Shi, S. Xia, Z. Ni and X. Xiao, *RSC Adv.*, 2015, **5**, 34319–34326.
27 W. Liu, Y. Yang, L. Chen, E. Xu, J. Xu, S. Hong, X. Zhang and M. Wei, *Appl. Catal., B*, 2021, **282**, 119569.
28 R. Li, W. Yao, Y. Jin, W. Jia, X. Chen, J. Chen, J. Zheng, Y. Hu, D. Han and J. Zhao, *Chem. Eng. J.*, 2018, **351**, 995–1005.
29 H. Wang, Q. Luo, W. Liu, Y. Lin, Q. Guan, X. Zheng, H. Pan, J. Zhu, Z. Sun, S. Wei, J. Yang and J. Lu, *Nat. Commun.*, 2019, **10**, 4998.
30 Y. Bonita, T. P. O'Connell, H. E. Miller and J. C. Hicks, *Ind. Eng. Chem. Res.*, 2019, **58**, 3650–3658.

© 2022 The Author(s). Published by the Royal Society of Chemistry